Chapter 4

MACRO-EM

3-D Macroscale Electromagnetic Particle Simulation Method for Large Space-Scale, Low Frequency Plasma Phenomena

Motohiko Tanaka

Summary

A new generation, electromagnetic particle simulation method is described which is quite suitable for studies of large time-and-space (MHD) scales, kinetic plasma phenomena in multi-dimensions. The "closely-coupled field-particle (CCFP) equations" are derived to realize large-scales simulations with aid of backward time-decentering and guiding center approximation to the electron perpendicular motion. Here an algorithm of the proto-type code which is implemented for simulating homogeneous plasmas is presented together with several physics applications.

4.1 Introduction

As is well-known, there is a giant gap in space and time between the microscopic (kinetic) and macroscopic (magnetohydrodynamic, MHD) regimes of the plasma phenomena. Neither the traditional particle nor MHD fluid codes were capable of simulating plasma waves and instabilities which occur between these two regimes.

Nevertheless, many important and interesting phenomena in space and fusion plasmas belong to this intermediate regime. For example, understanding of anomalous transport in the magnetically confined plasmas is of vital importance for the success of the magnetic fusion project but its mechanism is not well understood. In space plasmas, there are varieties of phenomena that belong

to this "macroscale and kinetic" regime. Typical of them are the magnetosonic shocks, magnetic reconnection and kinetic Alfven wave which shows substantial wave-particle interactions due to its longitudinal electric field.

Extensive efforts have been made in the 1980's, especially in the United States and Japan, to develop the simulation tools which enable us studies of the large space-scale, and low frequency plasma phenomena where kinetic effects are non-negligible or important. After the decade of R&D, it turned out that quite promising and useful among them are the "moment implicit" method, the "macroscale electromagnetic" method and the "gyrokinetic" particle method. The first method derives fluid-like moment equations to predict the future electromagnetic field using the lowest two velocity moments. This code known as "the VENUS code" [Brackbill and Forslund, 1982] was developed in Los Alamos National Laboratory in early 80's. This method was successfully applied to simulate laser irradiation and various beam-plasma processes [Forslund and Brackbill, 1982].

The macroscale electromagnetic particle simulation method [Tanaka, 1988] (HIDENEK) which was developed by the author has many favorable common features with the VENUS code and its upgrade (CELEST), for doing large time-and-space scale simulations; both of the codes adopt the backward time-decentering. The difference is that the macroscale particle code and CELEST use the particle nature directly that is contained in the Newton-Maxwell equations. The large time-and-space characteristics are realized by virtue of the backward time-decentering and the full-implicitness of the "closely-coupled field-particle (CCFP) equations", which are the equations to determine the future electromagnetic field. Thus in a technical sense, the macroscale particle simulation is the "closely-coupled implicit method."

An intermediate, "semi-implicit" version of the macroscale particle code was completed by 1986. This version of the code was applicable to studies of inhomogeneous plasmas even with the magnetic null points. Varieties of plasma phenomena were studied using this code, such as excitation of the kinetic Alfven wave /plasma heating [Tanaka, 1989] (Sec. 4) and current-beam injection /kink instability [Tanaka, 1986].

Although these studies were virtually the first attempts that have ever been made by the kinetic simulation method of general purposes, the time step was limited to $\omega_{pe}\Delta t \leq 1$ due to a simple-minded use of the predictor-corrector method; the future current density was predicted explicitly. Later in 1987, the full-implicit version of the macroscale particle code which deals with homogeneous plasmas was developed. The validity of this code was extensively studied and verified both in analytical and numerical ways [Tanaka, 1988]. An advanced version of the code that can be applied to multi-dimensional, inhomogeneous plasmas will be described in a separate literature [Tanaka, 1992].

It is noted in passing that the macroscale particle method is technically different from the magnetostatic (Darwin) code which neglects the displacement

Table 4.1: Characteristics of Macroscale Particle Simulation Code.

- Large time and space-scales:
  $\omega_{pe}\Delta t \gg 1$, $\omega_{ce}\Delta t \gg 1$, and $\Delta x/(c/\omega_{pe}) \geq 1$.
- Fully electromagnetic.
- Multi-dimensions in any geometry (Cartesian, cylinder, torus).
- Inhomogeneous density profile and arbitrary magnetic field structure.
- Fully kinetic:
  - ions: 3-D motion
  - electrons: parallel direction → 1-D motion with $(-\mu\nabla_{\parallel}B)$ force.
    perpendicular direction → guiding-center approximation
    ($\mathbf{E}\times\mathbf{B}$, ∇B and curvature drifts)

→ Resonance effects (Landau, cyclotron resonances)
Orbit effects : finite Larmor radius effects
diamagnetic current
banana orbit...
Longitudinal particle transport
} included.

current $\partial\mathbf{E}/\partial t$. The latter appears to be quite simple but actually requires complete separation of the transverse component of the current density from the longitudinal one for numerical stability. This is almost impractical to do in the real (configuration) space.

The concept of the gyrokinetic method [Lee, 1987] which was motivated in the Princeton Plasma Physics Laboratory is different from the previous two methods in the point that it is based on the smallness ϵ-ordering concerning the wavelength, frequency and amplitude of the electromagnetic field. Many insignificant terms are truncated in the original kinetic equations following the ordering. Therefore, this code should be correct and efficient as far as the smallness ordering assumptions are satisfied. However, when the assumptions become marginally satisfied, many correction terms need be taken into account which may degrade the advantage of the code.

Let us concentrate our attention to the simulations of low frequency phenomena. For this purpose, all the electron time scales, ω_{pe}, ω_{ce}, may be better eliminated. The characteristic features of the top-of-the-line version of the macroscale particle code - HIDENEK, are summarized in Table 4.1. The important feature here is that low frequency, electromagnetic (electrostatic, of course) waves and structures with $\omega\Delta t \ll 1$ are properly reproduced (ω: characteristic frequency). The Landau and cyclotron resonance effects are retained in the code. Since full particle dynamics is taken into account for the ions and for the parallel part of the electron motion on top of the perpendicular drifts, various

orbit effects of particles listed in Table 4.1 are well reproduced by the macroscale particle simulation. Moreover, the code is numerically stable both in the linear and nonlinear stages of simulations by virtue of simple backward-decentering. These characteristic features make the macroscale particle simulation method quite suitable for studies of nonlinear dynamics of large time-and-space scale, kinetic plasma phenomena.

In the next section, an algorithm of the proto-type macroscale particle simulation code is to be described. Several physics applications to the large-scale, kinetic problems will be shown in Sec. 3 and 4. The advanced version of the code with its applications will be found in the separate publication [Tanaka, 1992].

4.2 General Algorithm

4.2.1 Field and particle equations

The foregoing characteristic features of the macroscale particle code can be realized by introducing a slightly backward time-decentering both into the Maxwell equations and the equations of motion of particles [Tanaka, 1988]. The Maxwell equations with time level suffices are given by

$$\frac{1}{c}\left(\frac{\partial \mathbf{E}}{\partial t}\right)^{n+1/2} = \nabla \times \mathbf{B}^{n+\alpha} - \frac{4\pi}{c}\mathbf{j}^{n+\gamma}, \tag{4.1}$$

$$\frac{1}{c}\left(\frac{\partial \mathbf{B}}{\partial t}\right)^{n+1/2} = -\nabla \times \mathbf{E}^{n+\alpha}, \tag{4.2}$$

$$\nabla \cdot \mathbf{E}^{n+1} = 4\pi\rho^{n+1}, \tag{4.3}$$

$$\nabla \cdot \mathbf{B}^{n+1} = 0. \tag{4.4}$$

The equations of motion for the ions are written

$$\frac{d\mathbf{v}_j^{n+1/2}}{dt} = \frac{e_i}{m_i}\left[\mathbf{E}^{n+\alpha}(\mathbf{x}_j) + \frac{\mathbf{v}_j^{n+1/2}}{c} \times \mathbf{B}^{n+\alpha}(\mathbf{x}_j)\right], \tag{4.5}$$

$$\frac{d\mathbf{x}_j^{n+1/2}}{dt} = \mathbf{v}_j^{n+1/2}. \tag{4.6}$$

By contrast, the equations of motion for the electrons are split into the parallel and perpendicular parts as

$$\frac{dv_{\parallel j}^{n+1/2}}{dt} = \frac{(-e)}{m_e}E_{\parallel}^{n+\alpha}(\mathbf{x}_j), \tag{4.7}$$

$$\frac{d\mathbf{x}_j^{n+1/2}}{dt} = (\mathbf{v}_{\parallel j}^{n+1/2} + \mathbf{v}_{\perp j}^{n+\alpha}),$$

$$\mathbf{v}_{\perp j}^{n+\alpha} = c\left(\frac{\mathbf{E} \times \mathbf{B}}{B^2}\right)^{n+\alpha}(\mathbf{x}_j) \tag{4.8}$$

where $\mathbf{b} = (\mathbf{B}/B)$ is the unit vector along the magnetic field line, and the direction of the parallel velocity of the electrons is defined as

$$\mathbf{v}_{\|j}^{n+1/2} = v_{\|j}^{n+1/2}\mathbf{b}^{n+1/2}(\mathbf{x}_j). \tag{4.9}$$

In the present proto-type algorithm which is applicable to the homogeneous plasmas, only the $E \times B$ drift is incorporated in the perpendicular motion of the electrons. (Refer to Ref.13 for the advanced one.) The parameters α and γ are the implicitness parameters that are slightly larger than $\frac{1}{2}$.

The decentering shift of the time level in the curl terms of Eqs.(4.1), (4.2) causes damping of light waves with high frequencies. The damping of high frequency plasma waves is caused by the decentering shift of the field's time level in the equations of motion. It has been proved both analytically and numerically that decentering shift of the $E \times B$ term in Eq.(4.8) is virtually a necessary condition for the numerical stability [Tanaka, 1988] of the code.

It should be noted that the guiding-center approximation is adopted just for the "perpendicular" part of the electron motion for the purpose of eliminating the electron time scale ω_{ce}. By contrast, the ion and electron parallel motions are traced exactly as the particle species. These treatments facilitate the present code to study kinetic transport in magnetically confined fusion plasmas for which the relation $\omega_{ce} \sim \omega_{pe} \gg \omega_{ci}$ generally holds.

Just as a reminder. When we need to treat the plasmas with the magnetic-nulls, the electrons can be treated as the fully-kinetic species like the ions. The algorithm for this situation becomes much simpler than the present one with the guiding-center formula. It is also optional to introduce the guiding-center approximation to the ions; it may enable us simulations with a yet larger time scale with $\omega_{ci}\Delta t > 1$ at an expense of some physics on ions.

4.2.2 Equations in the finite difference form

The techniques that make the implicit algorithm feasible are presented here. The equations of motion for the ions in the finite difference form are written

$$\mathbf{v}^{n+1} = \mathbf{v}^n + \Delta t \frac{e_i}{m_i}\left[\mathbf{E}^{n+\alpha}(\tilde{\mathbf{x}}^{n+\gamma}) + \frac{\mathbf{v}^{n+1/2}}{c} \times \mathbf{B}^{n+\alpha}(\tilde{\mathbf{x}}^{n+\gamma})\right]. \tag{4.10}$$

(The particle index is suppressed hereafter.) If Eq.(4.10) is solved in terms of $\mathbf{v}^{n+1}$ using the interpolation $\mathbf{v}^{n+1/2} = \frac{1}{2}(\mathbf{v}^n + \mathbf{v}^{n+1})$, then we have

$$\begin{aligned}
\mathbf{v}^{n+1} &= \mathbf{v}^n + \Delta t \frac{e_i}{m_i}\left\{\left(\mathbf{E}^{n+\alpha} + \frac{\mathbf{v}^n}{c} \times \mathbf{B}^{n+\alpha}\right)\right. \\
&\quad + \frac{\Delta t}{2}\frac{e_i}{m_i c}\left(\mathbf{E}^{n+\alpha} + \frac{\mathbf{v}^n}{c} \times \mathbf{B}^{n+\alpha}\right) \times \mathbf{B}^{n+\alpha} \\
&\quad \left. + \left(\frac{\Delta t}{2}\frac{e_i B}{m_i c}\right)^2 \mathbf{E}_{\|}^{n+\alpha}\right\} / \left[1 + \left(\frac{\Delta t}{2}\frac{e_i B}{m_i c}\right)^2\right], \\
\mathbf{x}^{n+1} &= \mathbf{x}^n + \Delta t\ \mathbf{v}^{n+1/2}.
\end{aligned} \tag{4.11}$$

Similarly, the equations for the electrons in the finite difference form are written

$$v_{\parallel}^{n+1} = v_{\parallel}^{n} + \Delta t \frac{(-e)}{m_e} E_{\parallel}^{n+\alpha}(\tilde{\mathbf{x}}^{n+\gamma}), \tag{4.12}$$

$$\mathbf{x}^{n+1} = \mathbf{x}^{n} + \Delta t\, [\mathbf{v}_{\parallel}^{n+1/2} + \mathbf{v}_{\perp}^{n+\gamma}(\tilde{\mathbf{x}}^{n+\gamma})]. \tag{4.13}$$

The field value is evaluated at the "predicted" position $\tilde{\mathbf{x}}^{n+\gamma} = \mathbf{x}^n + \gamma\Delta t\, \mathbf{v}_{(0)}^{n+1/2}$ where $\mathbf{v}_{(0)}^{n+1/2}$ is calculated by using just the known field values at $t = t^n$.

The Maxwell equations in the finite-difference form are written

$$\mathbf{E}^{n+1} - \mathbf{E}^{n} = c\Delta t \nabla \times \mathbf{B}^{n+\alpha} - 4\pi\Delta t\, \mathbf{j}^{n+\gamma}, \tag{4.14}$$

$$\mathbf{B}^{n+1} - \mathbf{B}^{n} = -c\Delta t \nabla \times \mathbf{E}^{n+\alpha}. \tag{4.15}$$

In order to avoid the Courant condition which severely restricts the size of the time step Δt against the given space grid interval, we have to derive an implicit equation. Elimination of $\mathbf{B}^{n+1}$ from Eqs.(4.14)(4.15) by using the linear interpolation of the field quantity to the non-integer time level:

$$\mathbf{E}^{n+\alpha} = \alpha\mathbf{E}^{n+1} + (1-\alpha)\mathbf{E}^{n}, \tag{4.16}$$

yields the equation that governs the future electric field

$$[\, 1 + (\alpha c\Delta t)^2 \nabla \times \nabla \times \,]\, \mathbf{E}^{n+1} = [\, 1 - \alpha(1-\alpha)(c\Delta t)^2 \nabla \times \nabla \times \,]\, \mathbf{E}^{n} + c\Delta t \nabla \times \mathbf{B}^{n} - 4\pi\Delta t\, \mathbf{j}^{n+\gamma}. \tag{4.17}$$

In the above equation, the major electromagnetic terms are those excluding the vacuum term (1.). However, for the electrostatic component, the major contribution arises from the longitudinal current and the unity term in the square bracket.

4.2.3 Coupled field-particle equations

Since the implicitness parameters must be chosen as $\alpha, \gamma > \frac{1}{2}$, the current density in Eq.(4.17) is unknown and needs to be predicted. This is the key of all the implicit algorithm which, for the macroscale particle simulation, is done by expressing the current density in terms of the electromagnetic field:

$$\mathbf{j}^{n+\gamma}(\mathbf{x}) = \sum_j e_j \mathbf{v}_j^{n+\gamma} S(\mathbf{x} - \bar{\mathbf{x}}_j^{n+\gamma}) \tag{4.18}$$

$$= \sum_{j=i} e_i \,[\mathbf{v}_j^n + \gamma\Delta t \frac{e_i}{m_i} \{ \left(\mathbf{E}^{n+\alpha} + \frac{\mathbf{v}_j^n}{c} \times \mathbf{B}^{n+\alpha} \right) + \frac{\Delta t}{2} \frac{e_i}{m_i c} \left(\mathbf{E}^{n+\alpha} + \frac{\mathbf{v}_j^n}{c} \times \mathbf{B}^{n+\alpha} \right) \times \mathbf{B}^{n+\alpha}$$

$$+\left(\frac{\Delta t}{2}\frac{e_i B}{m_i c}\right)^2 \mathbf{E}_{\parallel}^{n+\alpha}\}/\{1+\left(\frac{\Delta t}{2}\frac{e_i B}{m_i c}\right)^2\}]\ S(\mathbf{x}-\bar{\mathbf{x}}_j^{n+\gamma})$$
$$+\sum_{j=e}(-e)\ \{v_{\parallel j}^n+\gamma\Delta t\frac{(-e)}{m_e}E_{\parallel}^{n+\alpha}\ +\ \mathbf{v}_{\perp j}^{n+\alpha}(\bar{\mathbf{x}}_j^{n+\gamma})\}\ S(\mathbf{x}-\bar{\mathbf{x}}_j^{n+\gamma}).$$

Substitution of this expression into Eq.(4.17) with Eqs.(4.11)-(4.13) and (4.15) forms a closed set of the Courant-condition-free, implicit equations which are named "closely-coupled field-particle (CCFP) equations" .

The third and fourth equations of Maxwell equations, Eqs.(4.3)(4.4) are the conditions to determine the initial field and need not be used mathematically for $t > 0$. However, in reality, use of the space grids inevitably causes an assignment error to the longitudinal part of the current density. Therefore, a correction to the electric field is required [Langdon and Lasinski, 1979]. This is done by deriving the correction equation for the scalar potential part:

$$\mathbf{E} \ = \ \tilde{\mathbf{E}} - \nabla\delta\varphi, \tag{4.19}$$

where $\mathbf{E}$ is the true electric field, and $\tilde{\mathbf{E}}$ is the electric field before the correction (the solution of Eq.(4.17)). The Gauss equation (4.3) then yields an equation for $\delta\varphi$ as

$$-\nabla^2\delta\varphi \ = \ 4\pi\rho^{n+1} \ - \ \nabla\cdot\tilde{\mathbf{E}}^{n+1}. \tag{4.20}$$

Since the charge density at $t = t^{n+1}$ is unknown a priori in the implicit algorithm, the expansion [Langdon, 1979] is used to expand the charge density around the predicted position $\mathbf{x}_{(l)}^{n+1}$:

$$\begin{aligned}\rho^{n+1}(\mathbf{x}) &= \textstyle\sum_j\ e_j S(\mathbf{x}-\mathbf{x}_j^{n+1}) \\ &= \textstyle\sum_j\ e_j S(\mathbf{x}-\mathbf{x}_{(l)}^{n+1}) - \nabla\cdot\sum_j\ e_j\delta\mathbf{x}_j S(\mathbf{x}-\mathbf{x}_{(l)}^{n+1}).\end{aligned} \tag{4.21}$$

This expansion implies conservation of charge density. Here, $\delta\mathbf{x}_j = \mathbf{x}_j^{n+1} - \mathbf{x}_{(l)}^{n+1}$ with $\mathbf{x}_j^{n+1}$ being the true position, and $\mathbf{x}_{(l)}^{n+1}$ the position calculated using $\tilde{\mathbf{E}}^{n+1}$ and $\mathbf{B}^{n+1}$. Thus, $\delta\mathbf{x}_j$ depends only on $\delta\varphi$ and Eqs.(4.20)(4.21) constitute the equations to determine the correction scalar potential field.

4.2.4 Miscellaneous

In the macroscale particle simulation, all the physical quantites are normalized by the four basic units which are suitable for treating the electromagnetic phenomena; the length: c/ω_{pe}, time: ω_{pe}^{-1}, mass: m_e, charge: e as

$$\hat{x} = \frac{x}{c/\omega_{pe}}\ ,\ \hat{t} = \omega_{pe}t\ ,\ \hat{m}_j = \frac{m_j}{m_e}\ ,\ \hat{e}_j = \frac{e_j}{e}. \tag{4.22}$$

Other quantities are normalized as combinations of these basic units;

$$\hat{\mathbf{v}} = \frac{\mathbf{v}}{c},\ \hat{\omega} = \frac{\omega}{\omega_{pe}},\ \hat{\mathbf{E}} = \frac{e\mathbf{E}}{m_e c\omega_{pe}}\ ,\ \hat{\mathbf{B}} = \frac{e\mathbf{B}}{m_e c\omega_{pe}}. \tag{4.23}$$

Quantities with (^) are used in the simulation. With this normalization, the constant in the field equations is transformed as $(4\pi) \rightarrow (1/n_0)$ (n_0: the average particle number density per unit-length) and the light speed (c) disappears everywhere.

It should be noted that Eq.(4.18) and (4.21) include the summations over the product of the particles and fields which represent a coupling of the neighboring plasma elements through the electromagnetic field. These calculations are generally too expensive otherwise the following approximation is introduced to the coupling terms:

$$\begin{aligned} & \textstyle\sum_j e_j \mathbf{E}^{n+\alpha}(\mathbf{x}_j) S(\mathbf{x}-\mathbf{x}_j) \\ = \; & \textstyle\sum_j e_j \mathbf{E}^{n}(\mathbf{x}_j) S(\mathbf{x}-\mathbf{x}_j) + \alpha \sum_j e_j (\mathbf{E}^{n+1}-\mathbf{E}^{n}) S(\mathbf{x}-\mathbf{x}_j) \\ \cong \; & \textstyle\sum_j e_j \mathbf{E}^{n}(\mathbf{x}_j) S(\mathbf{x}-\mathbf{x}_j) + \alpha \rho(\mathbf{x})(\mathbf{E}^{n+1}-\mathbf{E}^{n})(\mathbf{x}) \end{aligned} \tag{4.24}$$

The summations through the particle list can be thus separated from the iteration cycle of the CCFP equations. Since the major contribution is contained in the "accurate" first term on the righthandside of (4.24), this approximation is quite acceptable. This point has been verified numerically [Tanaka, 1988] and some of which will be reproduced in Sec. 4. Analytic and numerical proofs of the macroscale particle simulation in general are fully described in Tanaka [1988].

There are several remarks. First, exactly identical expressions must be used in the particle movers and the corresponding CCFP equations. Violation to this rule always causes a rapid blowup of the code. Next, the time step Δt should be chosen as: $\omega_{ci}\Delta t \leq 0.4$ for the ion orbit tracking and $k_\parallel v_\parallel \Delta t \ll 1$. More severe restriction may be that the particles should not travel for more than a few grids during Δt for accuracy reasons.

4.3 Alfven-Ion-Cyclotron Instability

The first example of physics applications of the present code is a one-dimensional simulation of the Alfven-ion-cyclotron (AIC) instability. The AIC waves are driven unstable by the ion temperature anisotropy.

The AIC instability was investigated by many authors analytically [Davidson and Ogden, 1975] and numerically [Tanaka et al., 1983; Tanaka, 1985; Omura, 1985]. The dispersion relation of the AIC waves is given by

$$\begin{aligned} \omega^2 - c^2k^2 + \omega_{pe}^2\left(\frac{\omega}{kv_e}\right)Z(\xi_e) + \omega_{pi}^2\left(\frac{\omega}{kv_{i\parallel}}\right)Z(\xi_i) \\ - \omega_{pi}^2\left(1-\frac{T_{i\perp}}{T_{i\parallel}}\right)\left[1+\xi_i Z(\xi_i)\right] = 0, \end{aligned} \tag{4.25}$$

where $\xi_e = (\omega \pm \omega_{ce})/kv_e$, $\xi_i = (\omega \pm \omega_{ci})/kv_{i\parallel}$ with ω_{ce}, ω_{ci} being the electron and ion cyclotron frequencies and v_e, v_i the thermal speeds of the electrons and

ions, respectively. The perpendicular temperature of the ions, $T_{i\perp}$, is defined by

$$T_{i\perp} = 2\pi \int_{-\infty}^{\infty} dv_{\parallel} \int_{0}^{\infty} dv_{\perp} v_{\perp} \left(\frac{1}{2} m_i v_{\perp}^2\right) f_i(v_{\parallel}, v_{\perp}). \tag{4.26}$$

Here $f_i(v_{\parallel}, v_{\perp})$ is the velocity distribution function of the ions. When the perpendicular temperature is greater than the parallel one, *i.e.*, $(T_{\perp}/T_{\parallel})_i > 1$, then the AIC waves become unstable. The typical frequency is $\omega \sim \omega_{ci}$, the growth rate $\gamma \sim (\beta_{i\perp}/2)^{1/2}\omega_{ci}$ and the wavenumber $ck/\omega_{pi} \sim 1$. The aforementioed dispersion relation reveals that any ion distribution function with the same temperature anisotropy is equivalent for the AIC instability. The spectrum width of the unstable wavenumber and the maximum growth rate are the increasing functions of the $(T_{\perp}/T_{\parallel})_i$ ratio and the ion beta value [Davidson and Ogden, 1975].

In the previous simulations, hybrid particle codes were used which treated the electrons as the massless species [Tanaka, 1985; Omura et al., 1985]. In the present macroscale simulation, the electrons are treated as the particle species along the magnetic field line, whereas only the $E \times B$ drift term is included in the perpendicular direction.

Before starting the simulation, the initial velocities are given to the ions and electrons so that each of the species follows the Maxwell distribution. The temperature anisotropy of $(T_{\perp}/T_{\parallel})_i = 5 - 20$ is given to the ions. The other parameters chosen are the sytem size $L_z = 120c/\omega_{pe}$, the temperature ratio $T_{i\parallel}/T_e = 1$, the parallel beta value $\beta_{i,\parallel} = 8 \times 10^{-2}$, and the electron cyclotron frequency $\omega_{ce}/\omega_{pe} = 0.7$ which corresponds to $\omega_{ci}/\omega_{pi} = 0.1$ for $m_i/m_e = 50$ case. (Note that the electron cyclotron frequency does not appear in the simulation algorithm.) The number of the cells in the z-direction is 128, the number of particles for each species is 12,800 and the time step is $\omega_{pe}\Delta t = 20$. (A larger time step $\omega_{pe}\Delta t \approx 10^3$ is possible for $m_i/m_e = 1836$.)

The time histories of the perturbed magnetic and electric field energies are shown for $(T_{\perp}/T_{\parallel})_i = 20$ case in Figure 4.1(a) and (b), respectively. The instability grows exponentially from the initial noise level and saturates around $\omega_{ci}t \sim 40$. For the electric field, the initial noise level is dominated by the electrostatic field and the instability appears to emerge abruptly above the noise level at $\omega_{ci}t \sim 30$. The growth rate is measured to be $\gamma/\omega_{ci} \sim 0.44$ for the mode three with $ck/\omega_{pi} \sim 1.1$ which is in agreement with the linear theory of the AIC instability.

The time history of the ion temperature anisotropy, $(T_{\perp}/T_{\parallel})_i$, is shown in Figure 4.1(c). When the intensity of the perturbed magnetic field reaches a certain level, *i.e.*, $< \delta B^2 > /8\pi n T_i \sim 0.2$, the temperature anisotropy begins to decrease. This process occurs relatively in a short time scale, $13\omega_{ci}^{-1}$. The final value of the anisotropy, $(T_{\perp}/T_{\parallel})_i \cong 2$ is found to be almost independent of the initial temperature anisotropies; the measured final anisotropies are 2.0, 1.8 and 2.3 for the initial anisotropies of 5, 10 and 20, respectively.

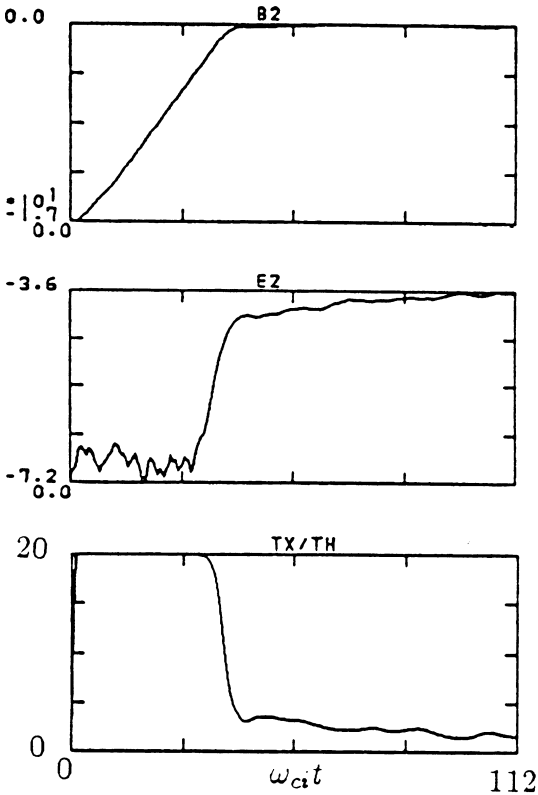

Figure 4.1: Time history of the perturbed magnetic (top) and electric (middle) field energies (in logarithmic scales) and the temperature anisotropy $(T_\perp/T_\parallel)_i$ (bottom, in linear scale) for $(T_\perp/T_\parallel)_{i0} = 20$ case.

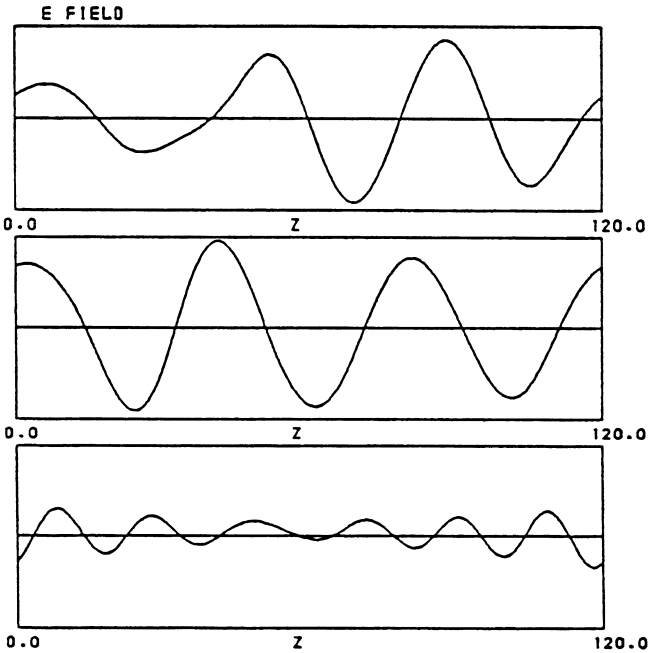

Figure 4.2: The three components of the electric field at $\omega_{ci}t = 42$.

The three components of the electric field at $\omega_{ci}t = 42$ are plotted in Figure 4.2. We can see a bit deformed sinusoidal wave of the mode number three. The electromagnetic components associated with the AIC instability, E_x and E_y, are already larger than the electrostatic component E_z at this stage. The mode number of the most unstable wave, four in the middle of the linear stage, has decreased to three at the beginning of the nonlinear stage of Figure 4.2.

A series of ion scatter plots in the $(v_z, v_\perp)$ space, (z, v_z) space and (z, ψ) space are shown in Figure 4.3(a)-(c), respectively. Here, $\psi = \tan^{-1}(v_y/v_x)$ is the phase angle of the perpendicular velocity. The ions undergo a remarkable pitch angle scattering during $\omega_{ci}t \sim 30 - 40$. This is most clearly found as the change in the $(v_z, v_\perp)$ space distribution from the needle-like distribution into a more isotropic round-shaped one at later times. This has been observed as the decrease in the temperature anisotropy in Figure 4.1(c).

More interesting observation is that the ions and electrons are highly modulated both in the velocity and configuration spaces. The ion modulation in the phase space (z, ψ) at the end of the linear stage $\omega_{ci}t \sim 42$ (Figure 4.3(c)) is in-phase with the magnetic perturbation and by 90 degrees out-of-phase with the electric field. This modulation of the velocity phase angle in accordance with the magnetic perturbation was also reported by the hybrid simulation [Tanaka

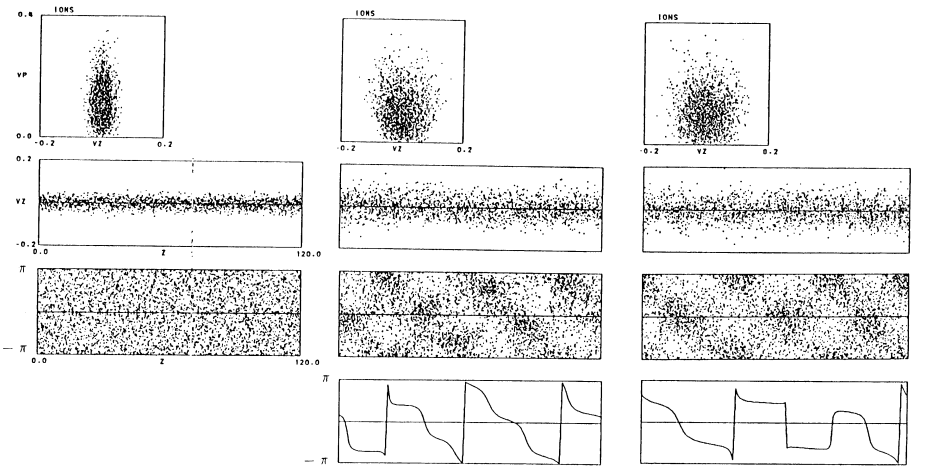

Figure 4.3: Ion scatter plots in the $(v_z, v_\perp)$, (z, v_z) and (z, ψ) spaces for $\omega_{ci}t = 0, 42$ and 56 (from top to bottom). The phase angle of the magnetic perturbation is shown at the bottom row.

et al., 1983]. However, the density modulation in the configuration space, which is shown in Figure 4.4 at $\omega_{ci}t \sim 56$ (right), develops only after the velocity modulation. This phenomenon has newly been noticed in the present macroscale particle simulation.

The overall results of the AIC instability have agreed well between the macroscale and hybrid simulations. The efficiency of the computation is twice better for the hybrid simulation in one-dimensional case. However, the hybrid simulation sometimes ends up with a blowup of the code in the middle of the nonlinear stage of the instability. The macroscale particle simulation can usually continue beyond this point and, what is more, it includes the electron dynamics.

4.4 Kinetic Alfven Waves

A two-dimensional application of the macroscale particle simulation is shown here. For this purpose, the kinetic Alfven wave (KAW) of a finite amplitude is initially loaded in a two-dimensional, bi-periodic magnetized plasma. Its propagation characterisitcs and the nonlinear stage are investigated [Tanaka, 1988].

The KAW posseses both the magnetohydrodynamic and kinetic natures due to its small perpendicular wavelength that is comparable to the ion gyroradius.

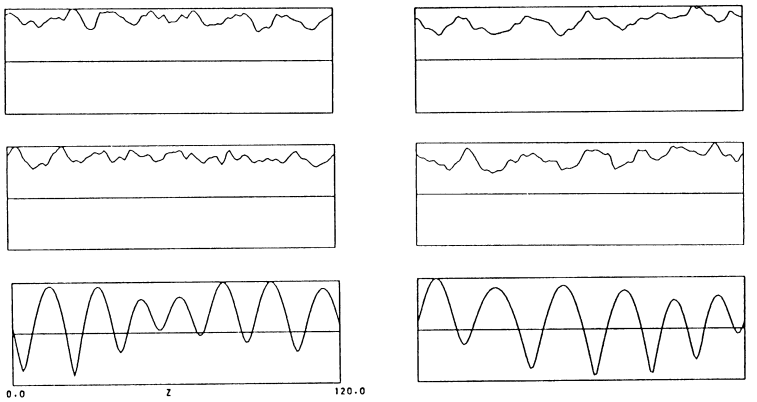

Figure 4.4: The spatial profiles of the ion, electron densities and the intensity of the magnetic field $|B^2|$ at $\omega_{ci}t = 42$ and 56 (from top to bottom, respectively).

This wave is accompanied by the longitudinal electric field and the density perturbation. The simulation system size is $L_x = 50c/\omega_{pe}$ and $L_z = 400c/\omega_{pe}$ with 32×64 cells. For this simulation, $\omega_{pe}\Delta t = 20$ is used to properly trace the ion cyclotron motion ($\omega_{ci}\Delta t = 0.4$ with $\omega_{ce}/\omega_{pe} = 1$ and $m_i/m_e = 50$).

The electromagnetic field of the kinetic Alfven wave is shown for $t/\tau_A = 2.6$ in Figure 4.5 where $\tau_A = 2\pi/k_\parallel v_A$. The major components of the electromagnetic field are E_x and B_y. These components always keep the same phase with each other as the wave propagates obliquely to the ambient magnetic field ($k_\perp/k_\parallel = 8$). The longitudinal electric field, E_z, is small but finite. In fact, the measurement of $< |E_z|^2 >$ gives a finite value, causing Landau resonance with the plasma particles.

Propagation of the kinetic Alfven wave is shown in Figure 4.6 where the wave keeps the initial sinusoidal wave form fairly well as it propagates obliquely in the (x, z) space. A close look at this figure reveals that the amplitude of this wave decreases in time. The phase speed and the damping rate of this wave, $\omega/k_z v_A \sim 1.08 - 1.6 \times 10^{-2} i$ agree very well with the linear theoretical value, $\omega/k_z v_A \sim 1.10 - 1.4 \times 10^{-2} i$ of the kinetic Alfven wave. Heating of the electrons along the ambient magnetic field is observed as a result of the wave damping (Fig 4.7). Flattening of the distribution function occurs in the velocity space at the resonance velocity $v_\parallel \cong \omega/k_\parallel$. This is another clue to the Landau damping of the kinetic Alfven wave.

Excitation of the kinetic Alfven wave by externally applied rf (current perturbation) at the edge of the plasma was studied by using 2-D macroscale particle code of the semi-implicit version [Tanaka et al., 1989]. In the simulation,

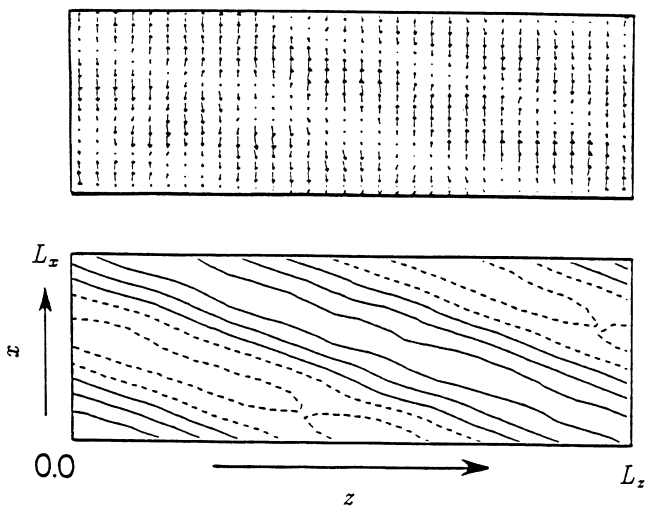

Figure 4.5: The electric field (E_x, E_z) (top) and the magnetic field B_y (bottom) of the kinetic Alfven wave at $t = 2.6\tau_A$.

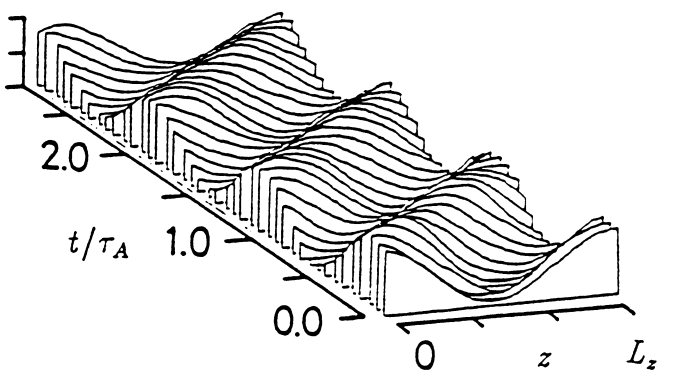

Figure 4.6: Propagation diagram of the kinetic Alfven wave where the magnetic perturbation B_y is shown as the function of (z, t) (a cross section at $x = const.$).

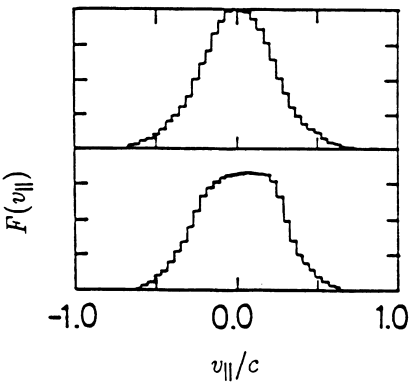

Figure 4.7: Heating of the electrons along the ambient magnetic field by the kinetic Alfven wave.

centrally peaked inhomogeneous density profile and the sheared magnetic field were given initially. Low frequency MHD perturbation which is evanescent in the plasma was excited for $t > 0$; this wave was observed to suffer from the Alfven resonance to generate the kinetic Alfven wave. Heating of the plasma was quantitatively investigated by changing the plasma beta value. The essence of the results is that in the low beta plasma, only the electrons absorb the wave energy through Landau resonance with the kinetic Alfven wave. When the plasma beta becomes comparable to unity, which occurs in the plasma sheet of the magnetosphere, the ions are heated to the same amount as the electrons. For the details of the results, refer to Tanaka et al. [1989].

4.5 Conclusion

In this chapter, the new generation particle simulation method, *i.e.*, "the macroscale particle simulation" has been described. This new simulation method enables us large time-and-space scale, kinetic plasma simulations in multi-dimensions. Two applications have been shown in Sec. 3 and 4 for the Alfven-ion-cyclotron instability and the kinetic Alfven wave. These two waves are the kinetic waves with MHD-scales.

As mentioned in Sec. 1, the macroscale particle simulation method - HIDENEK, belongs to the implicit particle methods and is technically classified as the "closely-coupled implicit method". The most advanced version of the code has now been implemented for studies of three-dimensional, inhomogeneous plasmas. Its detailed algorithm and 3-D application to the external kink

instability are found in Tanaka [1993] The author believes that this class of particle simulation methods will open up the new age of the computer simulation in space and fusion plasma physics.

Appendix: Flow of MACROS Code

A series of subroutines that constitute one time cycle of the macroscale particle simulation is shown here. The top part of the flow chart shows the initial loading of the particles and electromagnetic fields. The names in parentheses on the right are the subroutines for each procedure. The bottom part shows one cycle of the simulation.

Initial loading of particles and fields (INIT)

- Calculate constants, index tables (incl. FFT table).
- Generate particles in (x, y, z, v_x, v_y, v_z) space.
- Accumulate $\mathbf{j}$ and q (FULMOV; IPC= -1)
- Calculate initial electromagnetic field (EMFLD0)
- Conversion of electron velocity: $(v_x, v_y, v_z) \rightarrow (\mu, v_\perp, v_\parallel)$ (INITVE)

START of Time Cycle

Accumulate moments used in CCFP Eq. (FULMOV; IPC=1)

Solve the field $\tilde{\mathbf{E}}^{n+1}$, $\mathbf{B}^{n+1}$ with CCFP Eq. (EMFILD)

Accumulate moments used in $\delta\varphi$ Eq. (FULMV2)

Solve $\delta\varphi$ and correct $\tilde{\mathbf{E}}^{n+1}$ (ESCORR)

Advance particles to $\mathbf{x}^{n+1}$ and $\mathbf{v}^{n+1}$ (FULMOV; IPC=0)

Plasma diagnosis (DIAGNS)

If $t < t_F$ and (ctime) $<$ (ctime)$_F$, Goto START

END

References

Brackbill, J. U., and D.W.Forslund, An implicit method for electromagnetic plasma simulation in two dimensions, *J. Comput. Phys., 46*, 271, 1982.

Davidson, R. C., and J.M.Ogden, Electromagnetic ion cyclotron instability driven by ion energy anisotropy in high-beta plasmas, *Phys. Fluids, 18*, 1045, 1975.

Forslund, D.W., and J.U.Brackbill, Magnetic-field-induced surface transport in laser-irradiated foils,*Phys. Rev. Lett., 48*, 1614, 1982.

Langdon, A. B., and B.F.Lasinski, Electromagnetic and relativistic plasma simulation model, *Methods in Comput. Phys., 16*, 327, 1976.

Langdon, A. B., Analysis of the time integration in plasma simulation, *J. Comput. Phys., 30*, 202, 1979.

W.W.Lee, Gyrokinetic particle simulation model, *J. Comput. Physics, 72*, 243, 1987.

Omura Y., M.Abdalla, R.Gendrin and K.Quest, Heating of thermal helium in the equatorial magnetosphere: A simulation study, *J. Geophys. Res., 90*, 8281, 1985.

Tanaka, M., C. C. Goodrich, D.Winske and K.Papadopoulos, A source of the backstreaming ions in the foreshock region, *J. Geophys. Res., 88*, 3046, 1983.

Tanaka, M., Simulations of heavy ion heating by electromagnetic ion cyclotron waves driven by proton temperature anisotropies, *J. Geophys. Res., 90*, 6459, 1985.

Tanaka, M., and T.Sato, Macroscale particle simulation of relativistic electron beam injection into a magnetized plasma channel, *Phys. Fluids, 29*, 3823, 1986.

Tanaka, M., Macroscale implicit electromagnetic particle simulation of magnetized plasmas, *J. Comput. Phys., 79*, 209, 1988.

Tanaka, M., T. Sato and A. Hasegawa, Excitation of kinetic Alfven waves by resonant mode conversion and longitudinal heating of magnetized plasmas, *Phys. Fluids, B1*, 325, 1989.

Tanaka, M., A simulation of low-frequency, electromagnetic phenomena in kinetic plasmas of three dimensions, *J. Comput. Phys, in press*, 1993.